Progress In Electromagnetics Research C, Vol. 170, 162–173, 2026

PIER C

(Received 23 March 2026, Accepted 25 April 2026, Scheduled 12 May 2026)

A Miniaturized Multi-Resonant Wideband PIFA Design for Biomedical Applications

Hanwen Miao[1], Mengxing Liu[1], Le Song[1], Jingjing Shi[1,*],
Lijia Liu[2], and Jianqing Wang[2]

[1] *College of Medicine and Biological Information Engineering, Northeastern University, Shenyang 110169, China*
[2] *Graduate School of Engineering, Nagoya Institute of Technology, Nagoya 466-8555, Japan*

ABSTRACT: This paper presents a miniaturized implantable antenna with multi-resonances operating at the Medical Implant Communication Service (MICS) band (402–405 MHz) and Industrial, Scientific, and Medical (ISM) band (433.1–434.8 MHz, 868–868.6 MHz, and 902–928 MHz) for advanced biomedical applications. The proposed antenna is notably compact, occupying a volume of $10 \times 10 \times 1.27\,\text{mm}^3$ (equivalent to $127\,\text{mm}^3$). Multi-resonance frequencies are generated by incorporating a shorting pin and a meandered resonator structure. The proposed antenna exhibited wideband characteristics, with bandwidth ratios of 39.5% and 28.8% at 402 and 915 MHz, respectively. Moreover, the performance of the implantable antenna was further validated in different organs within a realistic human body model, such as the heart, stomach, small intestine, and colon. The practical performance of the fabricated antenna prototype was validated using a tissue-equivalent liquid phantom. Additionally, to evaluate the transmission performance under real-world scenarios, an on-body antenna matched with the implanted antenna was designed for an in-body to on-body transmission setup. Under the maximum safe input power of 25 μW, link budget analysis demonstrates that data can be transmitted at a rate of 10 Mbps over distances of 9.5 and 12 cm in the MICS and ISM bands, respectively. The simulated and experimental results verified the feasibility of substituting a realistic human model with a homogeneous muscle model in the design of an implantable antenna system and demonstrated a strong potential for diverse implantation scenarios and future biotelemetry applications.

1. INTRODUCTION

Implantable medical devices (IMDs) support an increasing number of diagnostic and therapeutic functions, including sensing, stimulation, monitoring, and drug delivery [1]. Among them, implantable antennas are key components that enable wireless communication with external medical devices [2]. Miniaturization is a critical challenge in the design of implantable antennas, because the implant devices must be compact enough to fit within the limited space available inside the human body [3]. Various antenna miniaturization techniques have been introduced, such as slot-based designs, spiral-structured configurations, and multi-layered antenna structures [4, 5]. In addition, the dielectric properties of human tissues are frequency-dependent and vary significantly across different body tissues, which further increase the complexity of implantable antenna design [6]. Different implantation scenarios can alter the resonant frequency and impedance bandwidth, potentially affecting the ability of the antenna to transmit and receive signals effectively. Increasing the antenna bandwidth always results in a trade-off with miniaturization. For example, the introduction of additional resonant arms or elements can enhance the bandwidth through multi-frequency operation [7, 8], but it often comes at the cost of increased size, which is counterproductive for implantable applications. In comparison, Planar Inverted-F Antennas (PIFAs) offer an advantageous solution owing to their inherent miniaturized design and enhanced bandwidth capabilities [9]. Specifically, by incorporating a ground plane with a monopole structure, PIFAs enable multiple resonances, thus supporting a broader operating frequency range than standard monopoles. This makes them particularly suitable for medical devices that operate across various frequency bands, such as skin-implantable biotelemetry units, wireless capsule endoscopy (WCE) systems, and leadless pacemakers (LPs), all of which have seen the widespread adoption of PIFA technology in recent years [10–17].

Currently, a wide variety of frequency bands are used for implantable device communication. The Medical Implant Communication Service (MICS) band, which operates at 402–405 MHz, has been a popular choice because of its relatively low risk of interference with other wireless services [18]. However, given the power consumption constraints and need for prolonged battery life in implantable devices, they often operate in multiple modes, such as sleep and wake-up modes. This operational diversity necessitates an antenna that can resonate at multiple frequencies to adapt to these modes, leading to the exploration of additional frequency bands. Industrial, Scientific, and Medical (ISM) bands have also been considered for biotelemetry in implantable devices. The frequencies within these bands 433.1–433.8 MHz, 868–868.6 MHz, and 902.8–928.0 MHz. Research has been conducted to design antennas operating at these frequencies and evaluate their

---

* Corresponding author: Jingjing Shi (shijj@bmie.neu.edu.cn).

doi:10.2528/PIERC26032305

Published by THE ELECTROMAGNETIC ACADEMY

TABLE 1. Comparison of proposed antenna with prior works.

Reference	Size (mm^3)	Band (MHz)	Bandwidth	Gain (dBi)
This work	$10 \times 10 \times 1.27$	402	159 (39.5%)	−39.8
		915	275 (28.8%)	−26.2
[21]	$14 \times 7.5 \times 0.5$	402	64 (15.8%)	−40.85
		915	91 (10.1%)	−32.98
[22]	$15 \times 15 \times 1.27$	915	97 (10.6%)	−27
[23]	$\pi \times 10^2 \times 2.54$	402	150 (38.1%)	−34.08
[24]	$10 \times 12 \times 1.27$	402	170 (34.3%)	−35.2
[25]	$26 \times 54 \times 0.2$	915	42.21 (4.6%)	−11
[26]	$11.6 \times 10 \times 0.5$	402	65.36 (16.2%)	−39.66

performance. For instance, a compact circularly polarized rectangular patch antenna operating in the single 915 MHz ISM band was designed for biomedical applications [19]. Another study analyzed the radiation performance of miniature antennas suitable for head-implanted medical devices that operate in the MICS and ISM bands [20]. Furthermore, one study assessed the efficiency of an antenna system for skin-implantable biotelemetry units operating in the MICS and ISM bands [21]. However, most of the literature faces a critical challenge in that the practical bandwidths of the small antennas are limited by their miniaturized size. Therefore, to achieve antenna miniaturization with a wide bandwidth, a multi-resonant compact antenna with a wider bandwidth should be proposed for advanced biomedical applications.

Accordingly, in this study, a miniaturized, multiband planar PIFA is presented for biomedical applications. The antenna was notably compact, measuring $10 \times 10 \times 1.27\,\text{mm}^3$. The antenna is designed to resonate at multiple frequency bands across the MICS (402–405 MHz) and ISM (433.1–434.8 MHz, 868–868.6 MHz, and 902–928 MHz) bands. Compared with the most recent implantable antennas listed in Table 1, the proposed antenna achieved a wider bandwidth at each resonant frequency while maintaining a smaller size. The multi-band operation of the antenna provides dual-mode communication. Specifically, the MICS operating band allows data transmission, whereas the ISM band ensures sleep mode and waits for the reception of a wake-up signal. The dual-mode communication system conserves battery energy to extend the lifetime of implanted devices. To evaluate the transmission performance of the implantable scenarios, we also designed a well-matched wearable antenna that operates at 402–405 MHz and 902–928 MHz, respectively. Furthermore, manufacturing and measurement procedures were conducted for both implantable and wearable antennas. The consistency between the simulation and measurement results confirms the feasibility of the antenna system for in-body communication applications.

The remainder of this paper is organized as follows. The antenna design is described in Section 2. The operating environment and evaluation of the antenna performance are introduced in Section 3. The antenna system analysis and discussion are presented in Section 4, and the link budget analysis is presented in Section 5. Finally, the conclusions are presented in Section 6.

2. ANTENNA DESIGN

The exact geometry of the proposed planar Inverted-F antenna is shown in Fig. 1. The dimensions are $10 \times 10 \times 1.27$ mm ($127\,\text{mm}^3$). As shown in Figs. 1(a)–(b), the serpentine-shaped radiation patch and ground plane are printed on a Rogers RO3210 substrate with a thickness of 0.635 mm. The substrate material Rogers RO3210 has a dielectric constant and tangent loss of 10.2 and 0.0027, respectively. Fig. 1(c) shows another 0.635 mm thick layer, which is the same material as the substrate to provide insulation. In addition, the superstrate layer with high relative permittivity can also shorten the effective wavelength to support antenna miniaturization. A shorting pin (via) with a diameter of 0.5 mm is configured to connect from the ground layer to radiation patch. A 50 Ω coaxial probe with a diameter of 0.9 mm is adopted to feed the antenna along the diagonal direction. The multiband operation with enhanced bandwidth was achieved by introducing a resonator and moving via at the appropriate position ($X = 6$ mm, $Y = 3.5$ mm). The optimized parameters are summarized in Table 2.

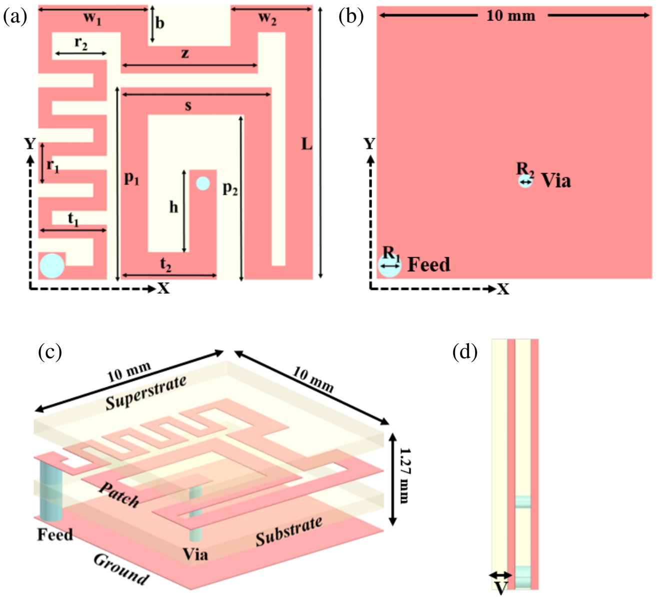

FIGURE 1. Proposed antenna geometry. (a) Radiating patch. (b) Ground plane. (c) Isometric view. (d) Side view.

TABLE 2. Detailed parameters of the implantable antenna (Units: mm).

Parameter	Value	Parameter	Value
w_1	4	t_1	2.5
w_2	3	t_2	3.5
r_1	1.5	z	5
r_2	2	s	5.5
p_1	7	b	1.5
p_2	6	V	0.635
h	3	R_1	0.9
L	10	R_2	0.5

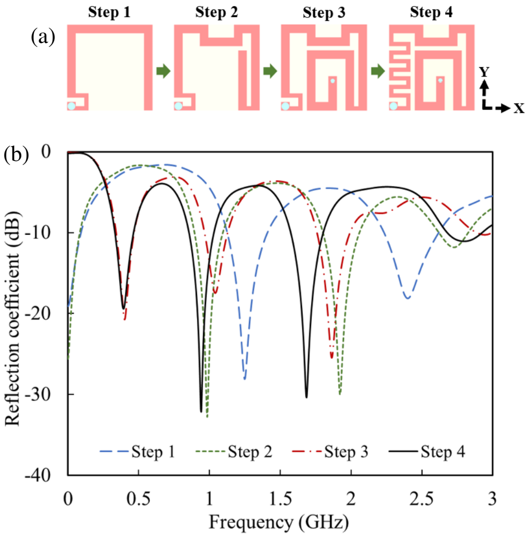

FIGURE 2. (a) Step-wise designing modifications. (b) Reflection coefficient S_{11} of the corresponding designing steps.

As shown in Fig. 2(a), the proposed multi-band antenna with wideband characteristics was designed and evolved through four steps. The reflection coefficient (S_{11}) comparison for the corresponding steps is shown in Fig. 2(b). As shown in step 1, the design of the proposed miniaturized antenna starts with a rectangular patch antenna. Owing to the introduction of a tortuous resonator, two resonant frequencies occur at 1.25 and 2.45 GHz, respectively. In step 2, by introducing a rectangular radiant plate, the resonant frequencies of the antenna shift slightly, but result in two stronger impedance matching at approximately 1 and 2 GHz, respectively. To ensure that the antenna operates within the target frequency bands, we inserted a via and a new resonant cavity on the antenna patch in step 3. The antenna generated a new resonant frequency at approximately 393 MHz and achieved acceptable impedance matching, thus producing a triple-band operation mode for the antenna. Finally, to cover the bandwidths of 868–868.6 MHz and 902–928 MHz, we introduced continuous and meandering slots above the feeding in step 4 and subsequently achieved impedance matching with a -10 dB bandwidth of 174 MHz (854–1028 MHz).

To better understand the working principle of the antenna, the current distributions of the metal radiation layer at 402 and 915 MHz are shown in Fig. 3. At 402 MHz, the full radiation patch is activated, and the current flows in the same direction from the feed to the via without changing its direction, indicating that all metal strips contribute to the low resonant frequency. In Fig. 3(b), the metal strip on the left side of the patch at the 915 MHz band has a higher surface current density, and the current changes direction only once at the lower right-hand corner of the patch, which indicates that good impedance matching is achieved at 915 MHz.

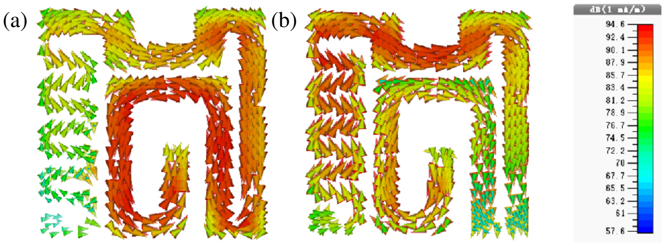

FIGURE 3. Current distributions on the radiating patch plane at (a) 402 MHz and (b) 915 MHz.

Moreover, the parameters affecting the antenna impedance matching were analyzed. First, based on the surface current distribution, it can be observed that the left-side meandered structure plays a dominant role in the resonance around 915 MHz. To further investigate its effect, a parametric study on the number of meander turns has been conducted. As shown in Fig. 4, it is evident that increasing the number of meander turns improves the impedance matching performance while simultaneously shifting the resonant frequency toward a lower frequency. This behavior can be attributed to the increase in the effective current path length, which leads to a lower resonant frequency and enhanced matching characteristics. Second, the position of the shorting via also plays a critical role in determining the antenna performance. By adjusting the via location, the electromagnetic coupling and current distribution within the antenna are modified, which in turn affects the input impedance and resonant characteristics. As shown in Fig. 5, different via positions can introduce additional resonances, shift the operating frequencies, and improve the impedance matching, enabling dual-band operation.

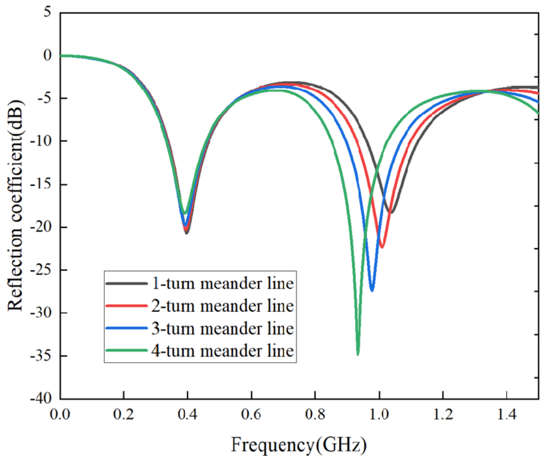

FIGURE 4. Effect of the number of meander turns on the reflection coefficient.

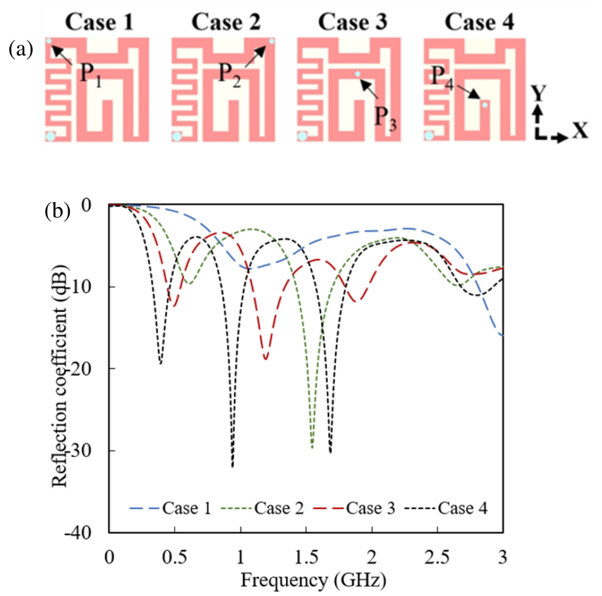

FIGURE 5. Via design steps and results: (a) Step-wise designing, (b) Reflection coefficient of the corresponding designing steps.

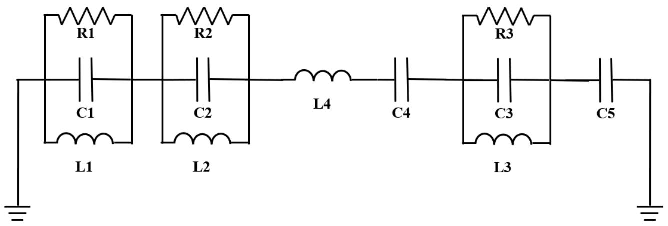

FIGURE 6. Equivalent circuit model of the antenna.

In addition, an equivalent circuit model was simulated using advanced design system (ADS) software, as shown in Fig. 6. The lumped components are precisely tuned to align the circuit's resonant frequencies with the operational frequencies of the antenna. The values of the lumped components are listed in Table 3. To validate the model, the simulated and measured reflection coefficients were compared with the circuit model results, as illustrated in Fig. 7. The comparison demonstrates close agreement among the three responses, and the equivalent circuit accurately replicates the reflection coefficient characteristics of the proposed antenna across its resonant frequencies, bandwidth, and overall variation trends.

TABLE 3. Values of the circuit model (Units: Ω, nH, pF).

Symbol	$R1$	$L1$	$C1$	$R2$	$L2$	$C2$
Value	20.06	0.1	2.87	68.59	7.05	14.37
Symbol	$R3$	$L3$	$C3$	$C4$	$L4$	$C5$
Value	250	1.1	11.99	14.75	5.46	21.36

3. ANTENNA PERFORMANCE

3.1. Operating Environment

Figure 8(a) shows the simulation setup of the in-body antenna implanted into a homogeneous muscle-equivalent model with dimensions of 100 mm × 100 mm × 100 mm, and the dielectric parameters of the model were frequency-dependent. In addition, we used a high-resolution, realistic numerical human model [27] to study the influence of the biological environment on antenna performance. We selected four typical implant positions: the heart, stomach, small intestine, and colon. Photographs of the fabricated antenna are shown in Fig. 8(b). The proposed antenna was measured in a liquid phantom, which was similar to the muscle-equivalent model in the simulation. The liquid phantoms were manufactured using deionized water, Triton (X-100), DGBE, and NaCl salt in different proportions [28]. The dielectric constants of the liquid phantom were characterized using the Keysight Dielectric Probe Kit. As shown in Fig. 9, the frequency-dependent relative permittivity and con-

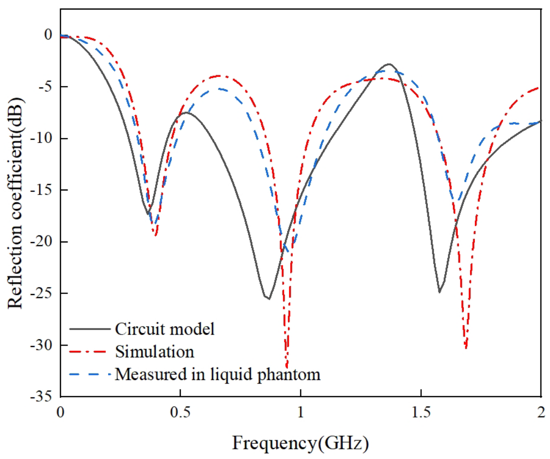

FIGURE 7. Circuit model, simulated and measured in liquid phantom S_{11} comparison.

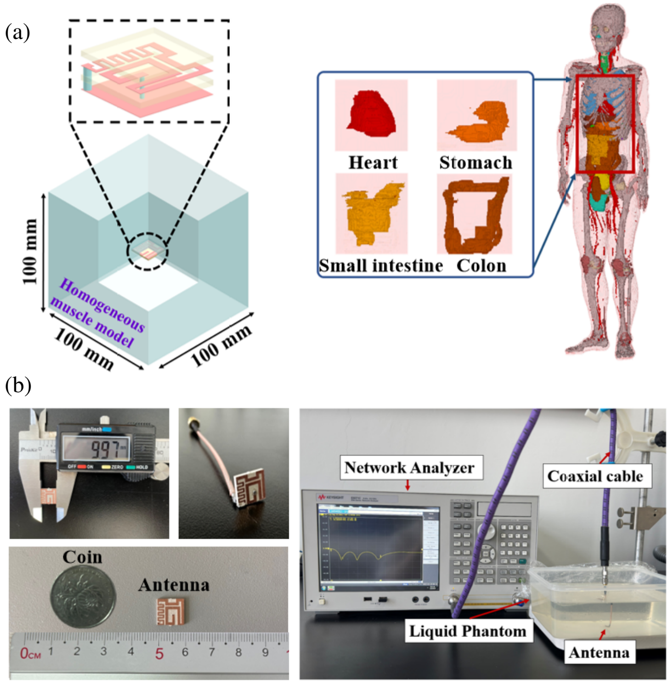

FIGURE 8. Simulations and measurements in implantation environments. (a) Simulation setups. (b) Measurement setups.

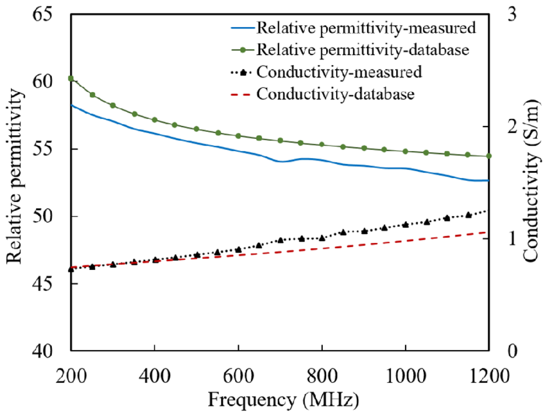

FIGURE 9. Comparison of the measurement results in the liquid phantom with those in the database.

ductivity of the liquid phantom are consistent with those of muscle tissue in the Gabriel open-access database within the 200–1200 MHz. Our proposed antenna was first designed and optimized using a homogeneous muscle-equivalent model in simulation, then evaluated using a realistic numerical human model numerically and a liquid phantom experimentally.

3.2. Reflection Coefficients of the Antenna

The comparison results of the reflection coefficient S_{11} under different operating environments are shown in Fig. 10. In the homogeneous muscle-equivalent model, the achieved impedance bandwidths ($S_{11} < -10\,\text{dB}$) were as follows: 124 MHz (334–458 MHz), 174 MHz (854–1028 MHz) and 224 MHz (1573–1797 MHz). The achieved bandwidth is sufficiently wide to cover four target frequency bands: MICS (402–405 MHz), ISM (433.1–434.8 MHz, 868–868.6 MHz and 902–928 MHz). Owing to the complexity of human tissues, the resonant frequencies slightly shifted downward within the four specific tissues of the realistic human model at both the first and second resonances. The antenna exhibited consistent reflection coefficients S_{11} within different types of human body tissues, confirming its stability in a realistic human body environment. In addition, the measured reflection coefficient S_{11} using the liquid phantom was compared with the simulations. As can be seen, the measured -10 dB impedance bandwidth are 159 MHz (323–482 MHz), 275 MHz (819–1094 MHz) and 180 MHz (1575–1755 MHz), respectively. Some frequency shifts between the measured and simulated resonances can be observed at higher frequencies, mainly because of the unavoidable manufacturing errors in the compact antenna size and impedance matching difficulties at higher frequencies. Notably, we found that the resonant frequencies at the MICS band are perfectly matched between realistic human tissue scenarios in simulations and the homogeneous muscle-equivalent model in experiments, and the resonant frequencies of human tissues at the ISM band shifted down by at most 9.3% from that of the homogeneous muscle-equivalent model but still covered the target frequency band. This means that the homogeneous muscle phantom model in both the simulations and experiments can provide an effective solution for the implantable small antenna design at the MICS (402–405 MHz) and ISM (902–928 MHz) bands if balancing the realistic human computational overhead in the simulations and the accuracy of the target resonant frequencies.

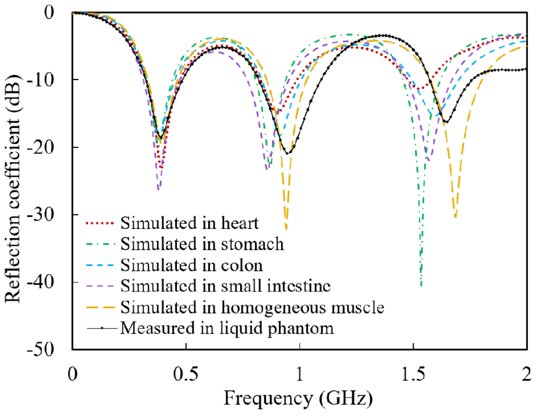

FIGURE 10. Comparison of simulated and measured S_{11} in different environments.

Specifically, the radiation efficiency is -40.8 dB at 402 MHz and -31.5 dB at 915 MHz, and the corresponding efficiency curves are presented in Fig. 11. It is well known that implantable antennas typically exhibit low radiation efficiency due to the highly lossy nature of biological tissues, which causes significant electromagnetic absorption and attenuation. Moreover, the stringent miniaturization requirements introduce increased ohmic losses and reduce the effective aperture, further degrading the overall radiation performance.

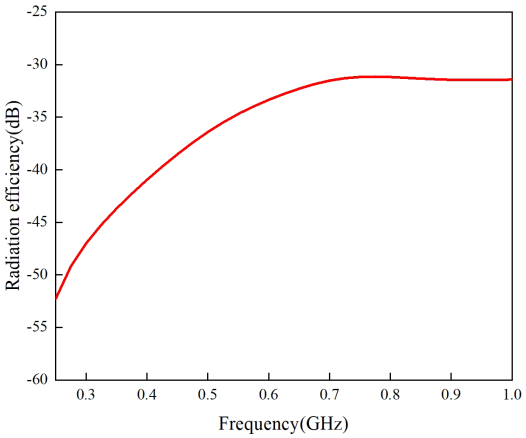

FIGURE 11. Radiation efficiency of the proposed antenna.

3.3. Radiation Patterns

The position and orientation of the implanted antenna traveling through the human body are uncontrollable, which poses a significant challenge to stable signal transmission. Therefore, an almost omnidirectional radiation pattern of the antenna is desired. The far-field radiation pattern and peak gain of the antenna were investigated in different human tissues. Fig. 12 shows the radiation patterns simulated at 402 and 915 MHz on two cross sections (xoz-plane and yoz-plane) when the antenna is implanted in the heart, colon, small intestine, and stomach. As can be seen, in most scenarios at two resonances, the radia-

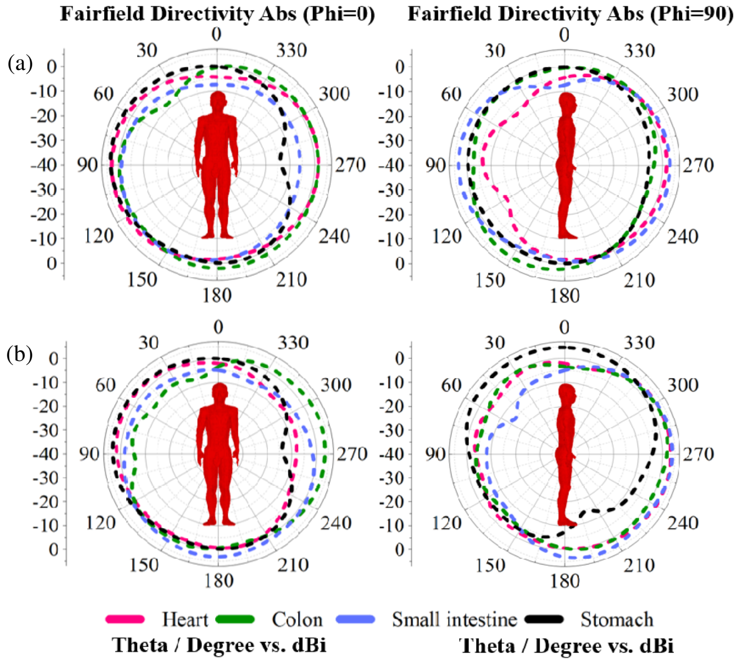

FIGURE 12. Radiation patterns of the proposed multiband implantable antenna. (a) 402 MHz. (b) 915 MHz.

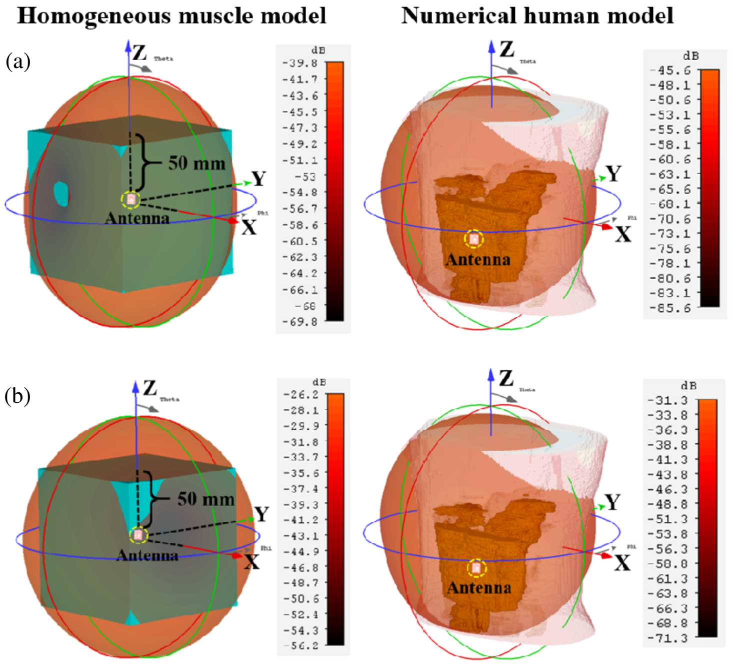

FIGURE 13. Comparison of far-field polar gain patterns. (a) 402 MHz. (b) 915 MHz.

tion patterns exhibit approximate omni-directivity. This feature benefits a stable signal transmission over various antenna orientations. The 3-D far-field gain radiation pattern is shown in Fig. 13. In Figs. 13(a) and (b), the far-field polar gain patterns of the antenna implanted in the homogeneous muscle model and numerical human model are compared at 402 and 915 MHz, respectively. The peak gain values of the antenna in the homogeneous muscle model were -39.8 and -26.2 dBi at the 402 and 915 MHz, respectively. The peak gain values of the antenna implanted in the realistic numerical human model is reduced by 5.8 dBi and 5.1 dBi at 402 MHz and 915 MHz, respectively, which was caused by the different dielectric properties of the complex human tissues. The relatively low gain at 402 MHz is mainly attributed to the highly lossy nature of biological tissues, which leads to significant electromagnetic absorption and attenuation, as well as additional dielectric and conductive losses and impedance mismatch effects. In addition, due to the long wavelength at this frequency, the antenna operates with a very small electrical size, inherently resulting in low radiation efficiency and degraded gain performance. Com-

TABLE 4. Simulated maximum average SARs and calculated maximum safety input power.

Tissue	Frequency (MHz)	SAR (W/kg)		Maximum input power (mW)	
		1-g	10-g	1-g	10-g
Heart	402	446.3	78.16	3.58	25.58
	915	337.6	67.51	4.73	29.62
Colon	402	595	73.62	2.68	27.16
	915	453.1	65.34	3.53	30.6
Stomach	402	412.3	75	3.88	26.6
	915	429.1	69.88	3.72	28.62
Small intestine	402	706.5	79.49	2.26	25.16
	915	632.9	74.33	2.52	26.9

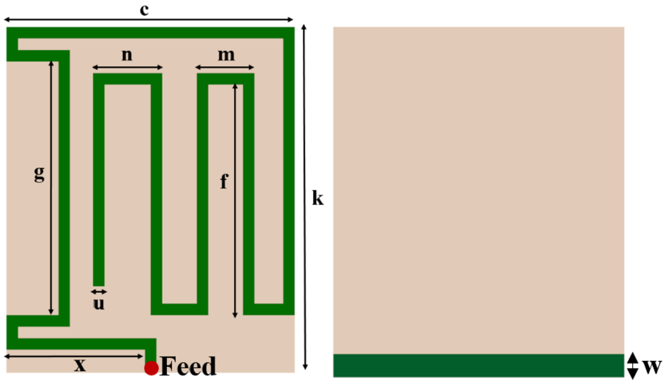

(a) (b)

FIGURE 14. On-body antenna geometry. (a) Radiating patch. (b) Ground plane.

pared with 915 MHz, the larger wavelength at 402 MHz further limits the radiation capability. Such a low gain is commonly observed in implantable antennas operating in the MICS band due to the combined effects of the lossy tissue environment and stringent miniaturization constraints.

3.4. Radiation Safety Evaluation

To ensure the safety of patients wearing IMDs, the IEEE C95.1-2005 standard limits the peak average specific absorption rate (SAR) of 1 g and 10 g of human tissue to less than 1.6 W/kg and 2 W/kg, respectively [29]. We conducted SAR evaluation at four different locations (heart, stomach, small intestine, and colon) in the human model. For these evaluations, the input power of the implanted antenna was set to 1 W. The SAR and maximum allowable input power values at the MICS band of 402 MHz and ISM band of 915 MHz for the four implant locations are listed in Table 4. Based on the 1-g peak SAR calculated in typical human tissues, the maximum safe input power of the antenna system operating in the MICS and ISM bands should not exceed 2.26 mW and 2.52 mW, respectively. However, for implantable antennas, the input power should be limited to -16 dBm (25 µW) [30], which is much lower than the calculated value. All the calculated maximum average SARs within different tissues are below the localized in-body exposure limits of 1.6 and 2 W/kg for 1-g and 10-g tissues, respectively.

4. TRANSMISSION CHARACTERISTIC ANALYSIS

4.1. On-Body Antenna Design

To evaluate the in-body to on-body transmission characteristics of the proposed transmitting antenna, we designed an on-body matched single-layer planar receiving antenna. As shown in Fig. 14, the size of the receiving antenna is $30 \times 25 \times 1.27\,\text{mm}^3$. The antenna has a single-layer planar structure consisting of a radiating element and a dielectric substrate using Rogers RO3210. The feed point of the antenna is located in the middle of the bottom edge of the antenna, and the radiation element of the antenna is a meandering monopole structure. The matched multi-resonances of the on-body antenna were achieved by modifying the structure of the resonator. The detailed parameters are summarized in Table 5.

TABLE 5. Detailed parameters of on-body antenna (Units: mm).

Parameter	Value	Parameter	Value	Parameter	Value
c	30	g	22	u	1
n	6	f	20	x	13
m	5	k	25	w	2

For the performance evaluation of the on-body antenna, as shown in Fig. 15(a), the on-body antenna was placed on the surface of the homogenous muscle model with a 1-mm gap in simulation and arranged on the surfaces of the liquid phantom and a realistic male in experimental measurements. The reflection coefficients S_{11} of different scenes were shown in Fig. 15(b). As observed from simulated results, the resonant frequencies of the antenna are 402 MHz and 915 MHz, and the -10 dB impedance bandwidths are 9 MHz (397–406 MHz) and 51 MHz (891–942 MHz), respectively, providing a good match with the proposed in-body antenna. From the measurement results of liquid phantom, wrist, chest, and back, the bandwidth of the antenna covers the target bands adequately, which indicates the feasibility of the proposed antenna within practical application scenarios.

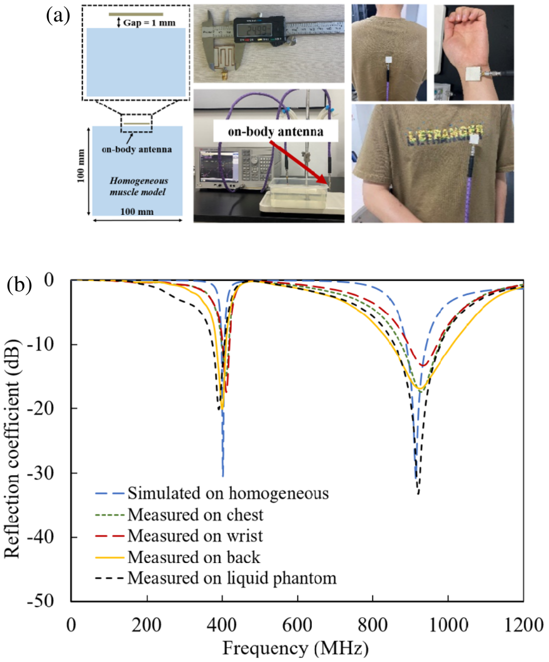

FIGURE 15. (a) Simulation and measurement scenarios. (b) S_{11} comparison in different implantation scenarios.

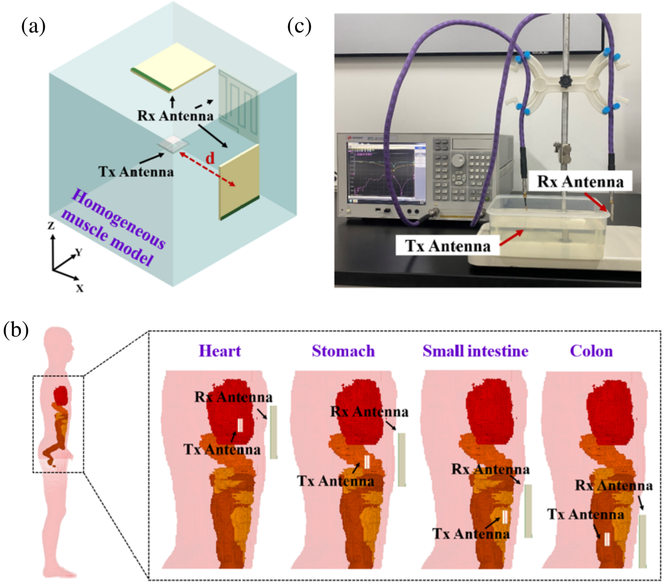

FIGURE 16. Transmission characteristic evaluation arrangement. (a) Simulation setup using a homogeneous muscle model (Rx antenna in x, y, and z-axis directions). (b) Simulation setup using a numerical human body model. (c) Measurement setup using a liquid phantom.

4.2. Transmission Coefficient of the Antenna System

4.2.1. S-Parameters

As shown in Fig. 16, to investigate the transmission coefficient S_{21} of the antenna system, the S-parameters are derived by presenting the in-body and on-body antenna with the homogeneous muscle model in simulation and the liquid phantom in measurement, respectively. As shown in Fig. 16(c), considering that the actual experiment will be limited by the opening direction of the liquid phantom container, this section selects the simulation and experimental results of the S-parameters in x-axis direction to compare the transmission performance of the antenna system. The simulation and actual measurement results of the S_{21} of the antenna system at a transmission distance of 2 cm are shown in Fig. 17. It is observed that the good match between in-body Tx antenna and on-body Rx antenna provides promising transmission coefficients. At the resonant frequencies of 402 MHz and 915 MHz, the simulation results of the maximum transmission coefficients S_{21} are -43.89 dB and -35.67 dB, respectively, and the actual measurement results are -31.62 dB and -39.19 dB. Same trends can be observed for simulation and measurement results, while the differences in S_{21} are mainly due to the unsatisfactory experimental environment and manufacturing error of the antennas.

As illustrated in Fig. 18, a realistic wireless data transmission scenario is experimentally established to validate the practical feasibility of the proposed implantable antenna. The system consists of a microcontroller-based transmitter and receiver, each integrated with a CC1101 operating in the MICS band (402–405 MHz). In the experimental setup, the in-body antenna is immersed in a tissue-mimicking liquid phantom to emulate the lossy biological environment, while the on-body antenna is positioned outside the phantom and connected to the receiver module. The transmission distance between the in-body transmitter and the on-body receiver is approximately 5 cm, forming a complete in-body to on-body wireless communication link. During operation, ECG signals are continuously modulated and transmitted from the in-body antenna at a transmitting power of 3 dBm (≈ 2 mW) and a data rate of 128 kbps. The signals propagate through the lossy medium and are successfully received, demodulated, and reconstructed at the external receiver without noticeable distortion or interruption, as shown in Fig. 18. These results demonstrate that the proposed implantable antenna enables stable and reliable wireless data transmission under realistic conditions. Moreover, the selected transmitting power complies with SAR safety constraints, remaining below the most stringent allowable input power among different tissue scenarios, thereby confirming its suitability for biomedical telemetry applications.

4.2.2. Distance Characteristics of Transmission Coefficient S_{21}

The transmission characteristic of the proposed antenna system is evaluated using the homogeneous muscle model, a numerical human model in simulation, and the liquid phantom in measurement, respectively. Firstly, as shown in Fig. 16(a), the on-body receiving antenna was placed on the surface of the homogeneous muscle model in three orientations which are x-, y-, and z-axis directions, while the in-body transmitting antenna was placed inside the model. Secondly, as shown in Fig. 16(b), the in-body antenna was implanted in different locations within the human body model, while placing the on-body antenna on the body surface in parallel. Seven implant positions, including the stomach, heart, small intestine, and colon, were selected for obtaining S_{21} under different distances. The simulated distance characteristics of S_{21} in different implantation scenarios are

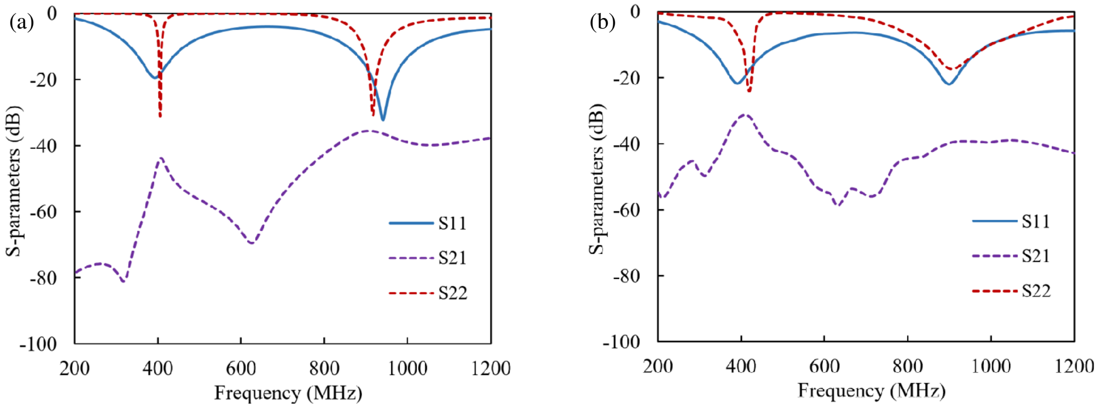

FIGURE 17. (a) Simulated and (b) measured results between S-parameters and frequency in MICS and ISM bands for x-axis direction.

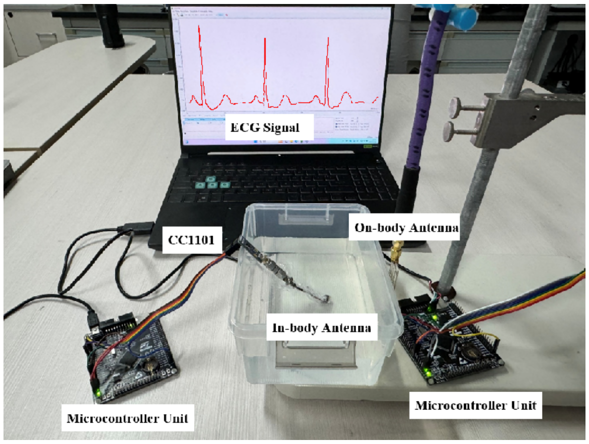

FIGURE 18. Wireless data transmission scenario setup.

shown in Fig. 19. It can be seen that with the increase of transmission distance, the S_{21} of the antenna system gradually decreases. At the same distance, the difference of S_{21} between the homogeneous muscle model and the numerical human model is within 5 dB, illustrating the transmission stability of the proposed antenna system within different biological environments. Finally, we conduct an experimental measurement to verify the transmission characteristic of the antenna system. As shown in Fig. 16(c), we moved the Tx antenna in parallel within the liquid phantom in x-axis while fixing the Rx antenna on the phantom surface, and the measured distance characteristics are obtained in Fig. 19. It can be seen that the measured S_{21} of the antenna system based on a homogeneous muscle-equivalent liquid phantom performs approximately 10 dB better than that of the simulated ones using a realistic human model at the MICS band of 402 MHz. This phenomenon may be due to the shadowing and diffraction effects of electromagnetic waves in a realistic human-sized measurement environment. However, the transmission characteristics at the ISM band of 915 MHz exhibit good accordance between the simulated human model and measured phantom model. The comparison results also reveal the feasibility of substituting a realistic human model with a homogeneous muscle model in implantable antenna system design and performance evaluations.

5. LINK BUDGET ANALYSIS

Link budget is the statistical analysis of all gains and losses throughout the entire process from the transmitter to the receiver through the transmission medium in a communication system [31]. In order to evaluate the communication quality of the antenna system, both the antenna systems operating at MICS and ISM bands are conducted for link budget analysis. The frequency-shift keying (FSK)-based impulse radio (IR) modulation with noncoherent detection proposed in our previous work [32] is used to calculate the link budget of the in-body to on-body channel. According to the calculation results in [32], given a threshold of the bit error rate (BER) equal to 10^{-3}, the required signal-to-noise power ratio (SNR) is 10.94 dB. The system margin M_a is defined as

$$M_a = \frac{E_b/N_0}{\left[E_b/N_0\right]_s} \tag{1}$$

where E_b and N_0 are unilateral power spectral densities of energy and thermal noise per bit, respectively. $[E_b/N_0]_s$ represents the E_b/N_0 required for the antenna system. If the E_b/N_0 of the system is greater than the required $[E_b/N_0]_s$, i.e., $M_a \geq 0$ dB, it proves that the wireless communication scheme is feasible. The greater the link margin of the system, the higher the reliability and stability of communication transmission. The link E_b/N_0 in decibel is given by

$$E_b/N_0 = P_t - PL - L_M - 10\lg\left(f_b\right) - N_{0,\text{dB}} \tag{2}$$

where P_t is the input power of the antenna, and PL is the path loss related to the implantation depth. The path loss can be obtained from the transmission coefficient $|S_{21}|$ of the antenna system in Fig. 14, which includes the gain of the transmitting antenna and receiving antenna. L_M represents miscellaneous loss, assuming 3 dB, and f_b represents the data rate. N_0 indicates the thermal noise power spectrum density in decibels, which is given by

$$N_{0,\text{dB}} = 10\lg\left(kT_0\right) + N_f \tag{3}$$

The relevant parameters are summarized in Table 6.

The link margin of the antenna system is calculated at data rates of 0.1 Mbps, 1 Mbps, and 10 Mbps with a communication distance of 1–12 cm inside the body. The calculated system

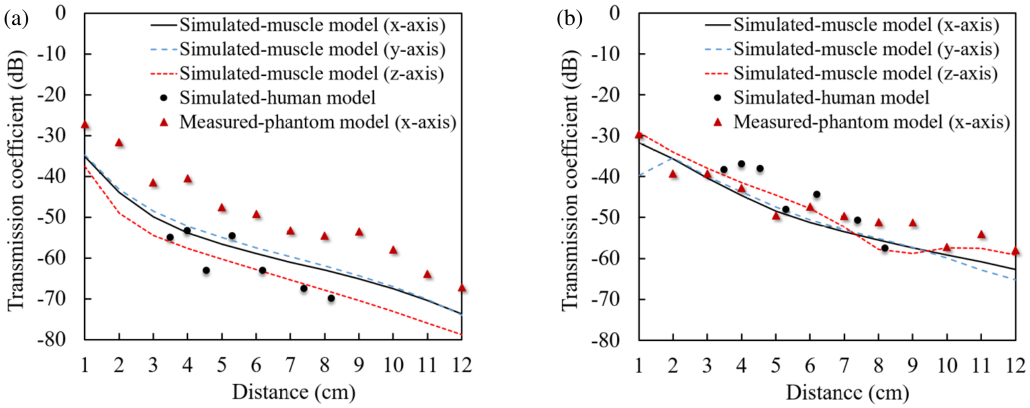

FIGURE 19. Distance characteristics of transmission coefficient S_{21} and transmission distance. (a) MICS band of 402 MHz. (b) ISM band of 915 MHz.

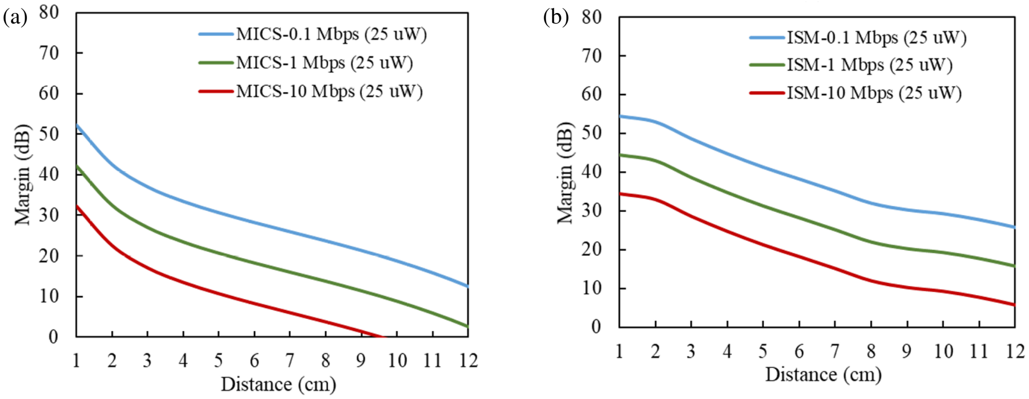

FIGURE 20. Link margin versus distance in (a) MICS band and (b) ISM band.

TABLE 6. Link budget parameters of the proposed antenna system.

Parameters	Variable symbol	Value
Frequency (MHz)	f	402/915
Transmitted power (dBm)	P_t	-16
Miscellaneous losses (dB)	L_M	3
Distance range (cm)	d	1–12
Receiver noise figure (dB)	N_f	6
Temperature (K)	T_0	300
Boltzmann constant (J/K)	K	1.38×10^{-23}
Bit error rate	BER	10^{-3}
Signal to noise power ratio (dB)	$[E_b/N_0]_s$	10.94

margins at MICS and ISM bands are shown in Fig. 20. As can be seen, when the data rate is 1 Mbps, and the transmission distance is 12 cm, the link margin of the antenna system in both the MICS and ISM bands is greater than 0 dB, indicating that reliable communication can be achieved at 1 Mbps. When the data rate is 10 Mbps, the maximum transmission distance of the system in the MICS band reaches 9.5 cm, while reliable communication can be ensured at a transmission distance of 12 cm in the ISM band. As a result, the link budget analysis demonstrates that the proposed antenna system is available for providing a highly reliable implant communication system. According to [33], a link margin (LM) greater than 20 dB is commonly used as the criterion for reliable communication. Based on this criterion, it is observed from Fig. 17 that when the data rate is 1 Mbps, the maximum transmission distance reaches 5.5 cm in the MICS band and 9.5 cm in the ISM band. When the data rate is 10 Mbps, the maximum transmission distance is 2.6 cm in the MICS band and 5.7 cm in the ISM band. As a result, the link budget analysis demonstrates that the proposed antenna system can provide a highly reliable implant communication link and meets the commonly accepted LM performance criterion reported in [33].

6. CONCLUSION

This paper proposes an innovative compact multi-resonant wideband Planar Inverted-F Antenna (PIFA), which operates across multiple frequency bands: MICS band (402–405 MHz) and ISM band (433.1–434.8 MHz, 868–868.6 MHz, and 902–928 MHz). A good agreement between the simulation and measurement results was observed. The measured -10 dB impedance bandwidths with a tissue-equivalent liquid phantom are 323–482 MHz (39.5%) and 819–1094 MHz (28.8%). In addition, the antenna performance was evaluated within various biological environments, including a homogeneous muscle-equivalent model, several typical organs, such as heart, stomach, small intestine, and colon within the realistic human model, respectively. Matching with an on-body antenna, stable reflection and transmission coefficients illustrate the robustness of the proposed antenna system applied in diverse implant applications. The homogeneous muscle-equivalent phantom model has been clarified as an effective substitute for a realistic human model at the MICS band with well-matched S_{11}, 10 dB variation of S_{21}, and ISM band with 9.3% frequency shift of S_{11}, well-matched S_{21}, respectively. Moreover, the radiation pattern for the proposed antenna has been evaluated. The results show that the antenna has stable performance, with peak gain values of -39.8 dBi and -26.2 dBi at 402 MHz and 915 MHz. The link budget analysis shows that the proposed antenna system can support a reliable communication at a data rate of 10 Mbps with the transmission distance covering 9.5 cm and 12 cm in the MICS and ISM bands, respectively. The proposed antenna is a promising candidate for future implantable medical devices requiring reliable wireless communication capabilities.

REFERENCES

[1] Shah, I. A., M. Zada, and H. Yoo, "Design and analysis of a compact-sized multiband spiral-shaped implantable antenna for scalp implantable and leadless pacemaker systems," *IEEE Transactions on Antennas and Propagation*, Vol. 67, No. 6, 4230–4234, Jun. 2019.

[2] Cui, W., R. Liu, L. Wang, M. Wang, H. Zheng, and E. Li, "Design of wideband implantable antenna for wireless capsule endoscope system," *IEEE Antennas and Wireless Propagation Letters*, Vol. 18, No. 12, 2706–2710, Dec. 2019.

[3] Xu, L.-J., Y.-X. Guo, and W. Wu, "Miniaturized dual-band antenna for implantable wireless communications," *IEEE Antennas and Wireless Propagation Letters*, Vol. 13, 1160–1163, 2014.

[4] Nikolayev, D., M. Zhadobov, L. L. Coq, P. Karban, and R. Sauleau, "Robust ultraminiature capsule antenna for ingestible and implantable applications," *IEEE Transactions on Antennas and Propagation*, Vol. 65, No. 11, 6107–6119, Nov. 2017.

[5] Liu, C., Y.-X. Guo, and S. Xiao, "Circularly polarized helical antenna for ISM-band ingestible capsule endoscope systems," *IEEE Transactions on Antennas and Propagation*, Vol. 62, No. 12, 6027–6039, Dec. 2014.

[6] Karacolak, T., R. Cooper, E. S. Unlu, and E. Topsakal, "Dielectric properties of porcine skin tissue and in vivo testing of implantable antennas using pigs as model animals," *IEEE Antennas and Wireless Propagation Letters*, Vol. 11, 1686–1689, 2012.

[7] Liu, C., Y.-X. Guo, and S. Xiao, "Compact dual-band antenna for implantable devices," *IEEE Antennas and Wireless Propagation Letters*, Vol. 11, 1508–1511, 2012.

[8] Xu, L.-J., Y.-X. Guo, and W. Wu, "Bandwidth enhancement of an implantable antenna," *IEEE Antennas and Wireless Propagation Letters*, Vol. 14, 1510–1513, 2015.

[9] Kim, J. and Y. Rahmat-Samii, "Implanted antennas inside a human body: Simulations, designs, and characterizations," *IEEE Transactions on Microwave Theory and Techniques*, Vol. 52, No. 8, 1934–1943, Aug. 2004.

[10] Zada, M. and H. Yoo, "A miniaturized triple-band implantable antenna system for bio-telemetry applications," *IEEE Transactions on Antennas and Propagation*, Vol. 66, No. 12, 7378–7382, Dec. 2018.

[11] Bakogianni, S. and S. Koulouridis, "A dual-band implantable rectenna for wireless data and power support at sub-GHz region," *IEEE Transactions on Antennas and Propagation*, Vol. 67, No. 11, 6800–6810, Nov. 2019.

[12] Shah, S. A. A. and H. Yoo, "Radiative near-field wireless power transfer to scalp-implantable biotelemetric device," *IEEE Transactions on Microwave Theory and Techniques*, Vol. 68, No. 7, 2944–2953, Jul. 2020.

[13] Faisal, F., M. Zada, A. Ejaz, Y. Amin, S. Ullah, and H. Yoo, "A miniaturized dual-band implantable antenna system for medical applications," *IEEE Transactions on Antennas and Propagation*, Vol. 68, No. 2, 1161–1165, Feb. 2020.

[14] Hayat, S., S. A. A. Shah, and H. Yoo, "Miniaturized dual-band circularly polarized implantable antenna for capsule endoscopic system," *IEEE Transactions on Antennas and Propagation*, Vol. 69, No. 4, 1885–1895, Apr. 2021.

[15] Li, R., Y.-X. Guo, and G. Du, "A conformal circularly polarized antenna for wireless capsule endoscope systems," *IEEE Transactions on Antennas and Propagation*, Vol. 66, No. 4, 2119–2124, Apr. 2018.

[16] Sharma, D., V. Kaim, B. K. Kanaujia, N. Singh, S. Kumar, and K. Rambabu, "A triple band circularly polarized antenna for leadless cardiac transcatheter pacing system," *IEEE Transactions on Antennas and Propagation*, Vol. 70, No. 6, 4287–4298, Jun. 2022.

[17] Faisal, F., M. Zada, H. Yoo, I. B. Mabrouk, M. Chaker, and T. Djerafi, "An ultra-miniaturized antenna with ultra-wide bandwidth for future cardiac leadless pacemaker," *IEEE Transactions on Antennas and Propagation*, Vol. 70, No. 7, 5923–5928, Jul. 2022.

[18] Liu, C., Y.-X. Guo, and S. Xiao, "A hybrid patch/slot implantable antenna for biotelemetry devices," *IEEE Antennas and Wireless Propagation Letters*, Vol. 11, 1646–1649, 2012.

[19] Xu, L.-J., Y.-X. Guo, and W. Wu, "Miniaturized circularly polarized loop antenna for biomedical applications," *IEEE Transactions on Antennas and Propagation*, Vol. 63, No. 3, 922–930, Mar. 2015.

[20] Kiourti, A. and K. S. Nikita, "Miniature scalp-implantable antennas for telemetry in the MICS and ISM bands: Design, safety considerations and link budget analysis," *IEEE Transactions on Antennas and Propagation*, Vol. 60, No. 8, 3568–3575, Aug. 2012.

[21] Gani, I. and H. Yoo, "Multi-band antenna system for skin implant," *IEEE Microwave and Wireless Components Letters*, Vol. 26, No. 4, 294–296, Apr. 2016.

[22] Zhang, K., C. Liu, X. Liu, H. Guo, and X. Yang, "Miniaturized circularly polarized implantable antenna for ISM-band biomedical devices," *International Journal of Antennas and Propagation*, Vol. 2017, No. 1, 9750257, Mar. 2017.

[23] Ganeshwaran, N., J. K. Jeyaprakash, M. G. N. Alsath, and V. Sathyanarayanan, "Design of a dual-band circular implantable antenna for biomedical applications," *IEEE Antennas and Wireless Propagation Letters*, Vol. 19, No. 1, 119–123, Jan. 2020.

[24] Zhang, X., L. Li, X. Zhang, Q. Zhao, and Y. Lu, "A dual band implantable antenna," in *2018 International Applied Computational Electromagnetics Society Symposium — China (ACES)*, 1–2, Beijing, China, 2018.

[25] Kam, K. A., V. Kumar, C. K. Lardner, I. Mollicone, D. Dumitriu, and I. Kymissis, "A fully integrable 915 MHz implantable antenna system for long-range telemetry in rodents," in *2023 IEEE MTT-S International Microwave Biomedical Conference (IMBioC)*, 55–57, Leuven, Belgium, 2023.

[26] Bahrouni, M., G. Houzet, H. Trabelsi, and T. P. Vuong, "A low profile dual band implantable antenna for biomedical applications," in *2023 22nd Mediterranean Microwave Symposium (MMS)*, 1–4, Sousse, Tunisia, 2023.

[27] Nagaoka, T., S. Watanabe, K. Sakurai, E. Kunieda, S. Watanabe, M. Taki, and Y. Yamanaka, "Development of realistic high-resolution whole-body voxel models of japanese adult males and females of average height and weight, and application of models to radio-frequency electromagnetic-field dosimetry," *Physics in Medicine & Biology*, Vol. 49, No. 1, 1–15, Dec. 2003.

[28] Yilmaz, T., T. Karacolak, and E. Topsakal, "Characterization of muscle and fat mimicking gels at MICS and ISM bands (402–405 MHz and 2.40–2.48 GHz)," in *XXIX General Assembly of International Union of Radio Science (URSI)*, Chicago, Illinois, USA, Aug. 2008.

[29] IEEE standard for safety levels with respect to human exposure to radio frequency electromagnetic fields, 3 kHz to 300 GHz, *IEEE Std C95.1-2005 (Revision of IEEE Std C95.1-1991)*, 1–238, Apr. 2006.

[30] Cheng, X., D. E. Senior, C. Kim, and Y.-K. Yoon, "A compact omnidirectional self-packaged patch antenna with complementary split-ring resonator loading for wireless endoscope applications," *IEEE Antennas and Wireless Propagation Letters*, Vol. 10, 1532–1535, 2011.

[31] Wang, J. and Q. Wang, *Body Area Communications*, Wiley, New York, NY, USA, 2013.

[32] Shi, J., H. Liu, X. Wang, J. Zhang, F. Han, X. Tang, and J. Wang, "Miniaturized dual-resonant helix/spiral antenna system at MHz-band for FSK impulse radio intrabody communications," *IEEE Transactions on Antennas and Propagation*, Vol. 68, No. 9, 6566–6579, Sep. 2020.

[33] Huang, J., X. Liu, Y. Fan, and Z. Ju, "Dual-band and left-/right-handed circularly polarized implantable antenna for arteriovenous grafts in hemodialysis," *IEEE Transactions on Antennas and Propagation*, Vol. 73, No. 10, 7207–7220, 2025.